XVII. Solid Propellant Engineering

PROPULSION DIVISION

A. Nondestructive Testing of 1-W, 1-A Electro-Explosive Devices, *V. J. Menichelli*

1. Introduction

A program is underway to study the response of various electro-explosive devices to the "transient pulse" and "thermal follow display" nondestructive tests. A description of the circuitry and the theory associated with these tests were reported in SPS 37-62, Vol. III, pp. 228–233. This article describes the isolation and dissection of a squib which displayed an abnormal response to the two nondestructive tests.

2. Test Results

During the tests, the dual bridgewire squib identified as #42901 displayed highly irregular and unstable heating curves for both bridgewire circuits. Due to the instability of response at the time of testing, no statistical data were taken. Figure 1 shows heating curves obtained by the transient pulse test. Included is a heating curve obtained on a squib from the same lot (#42906) which gave what is considered a normal response. Figure 2 shows heating curves obtained by the thermal follow display test and also a typically normal response expected from a healthy squib.

Examination of the transient pulse heating curves shows some sharp rapid changes early in the heating and later some slower more gradual changes. The same conditions are reflected in the thermal follow display curves. The early distortions in the heating curves are believed due to ohmic heating resulting from poor welds or bridgewire defects. The later more gradual changes in the heating curve are attributed to poor contact between the bridgewire and explosive material. A poor bridgewire weld results in high contact resistance, which is an important factor in generating the heating curve. A lack of intimate contact between the bridgewire and explosive material can cause non-uniform heat transfer resulting from wire expansion as the temperature rises.

3. Investigation

The squib was dissected to attempt to correlate the abnormal response which occurred during testing with

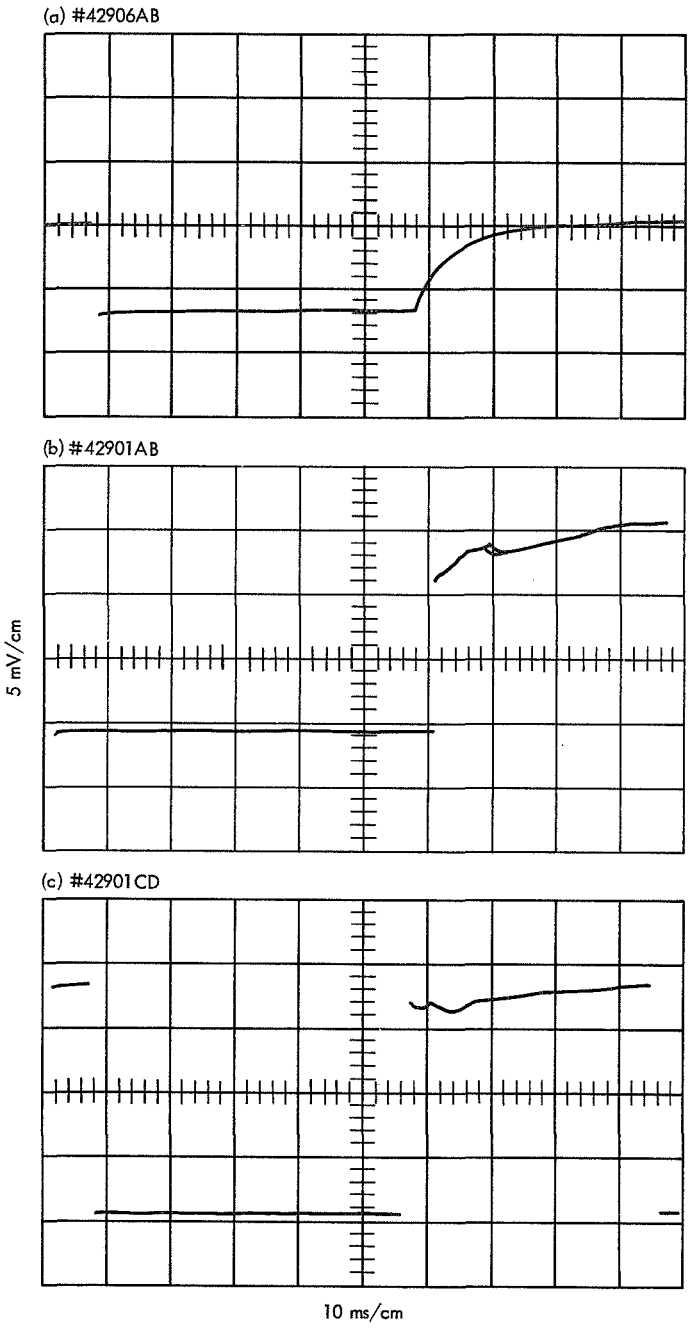

Fig. 1. Heating curves generated by the transient pulse technique

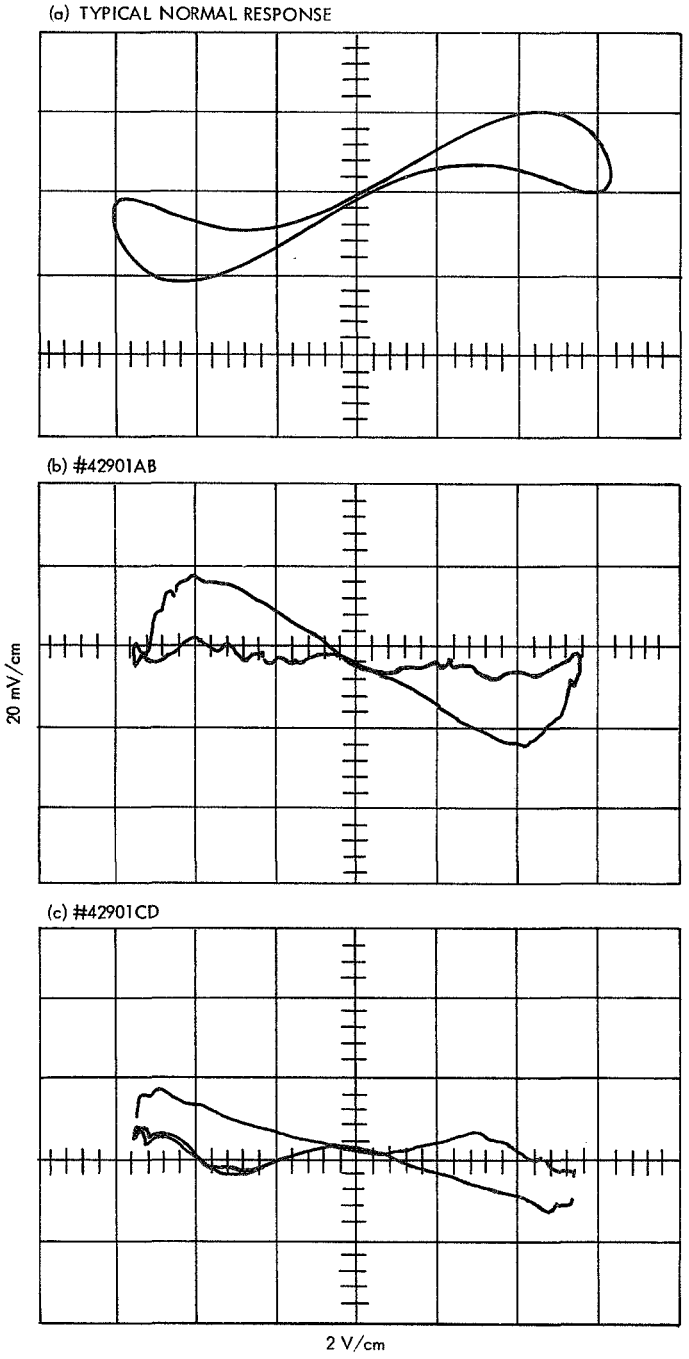

Fig. 2. Heating curves generated by the thermal follow display technique

some internal defect. Dissection began by carefully machining away the end seal from the squib and removing the base charge. Special care was taken not to disturb the matchhead material loaded on the bridgewire. It was observed that the density of the matchhead material was lower than good ordnance practice would dictate. The squib was then subjected to the transient pulse test, with the exception that the driving voltage was increased so as to heat the wire above the normal operating test temperature but not high enough to cause initiation. The pulsing at this level would stress the bridgewire beyond what it sees in a normal test. Also, the pulsing would continue for a much longer period of time. The purpose was to accelerate any defects to the point of failure. One would not normally use the transient pulse test in this manner when making a nondestructive measurement. However, for this application the equipment became an appropriate tool to study suspected faults. After approximately 15 min of pulsing, bridgewire AB opened without causing ignition of the matchhead. The same procedure was used on bridgewire CD, and after about 10 min, it also opened without causing the charge to initiate.

The next step in the investigation was the removal of the matchhead material from the bridgewire. This was carefully done by soaking out the material with acetone and cleaning with a camel hair brush. The material washed out quite easily, indicative of the low compaction density. The bridgewires and posts were examined microscopically. Examination of the AB bridgewire circuit showed that one end of the wire had been barely attached to the post (Fig. 3a). The weld was obviously very poor and the pulsing action of the transient pulse test caused it to fail. The other end of the circuit (Fig. 3b) showed the wire still welded to the post, but the weld is considered substandard. Bridgewire circuit CD showed a different failure mode. The bridgewire appeared to be welded securely at both ends (Figs. 4a and 4b). However, there appeared to be a necking down of the bridgewire at the inside weld which can be attributable to a wire defect or possibly corrosion. Figure 4c appears to show the open circuit resulting from a mechanical break. The break took place at the point where maximum stress was taking place due to the pulsing action.

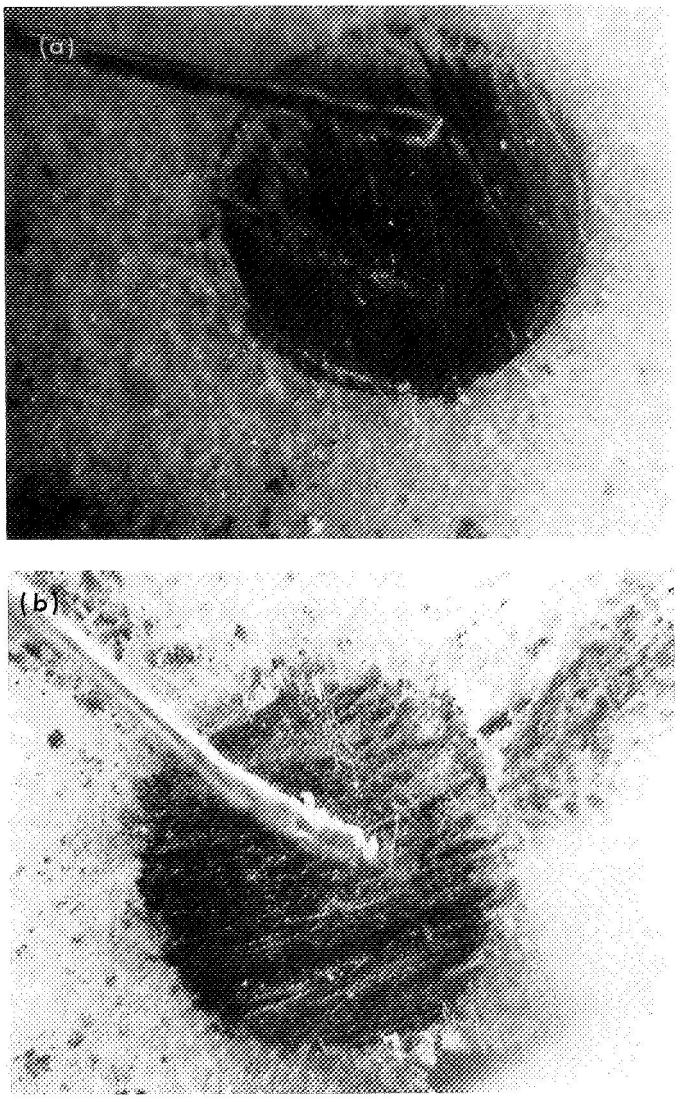

Fig. 3. Photo micrographs of AB bridgewire and posts for squib #42901

4. Conclusions

The results of this investigation, although not conclusive, certainly demonstrate that the observed abnormal heating curve effect can be related to a cause. The transient pulse and thermal follow display tests did indeed cull out an undesirable squib. It can be argued that this squib failed because of the unusual conditions under which it was tested. However, this and similar methods are valid in determining shelf life or ruggedness of a specific design. It is probable that the same or similar conditions could be encountered by temperature cycling from environments on earth or in space. Visual inspection of the welds showed that they were far from being adequate and could have failed from other causes such as vibration and shock. One would not want to use such a squib in a high reliability application.

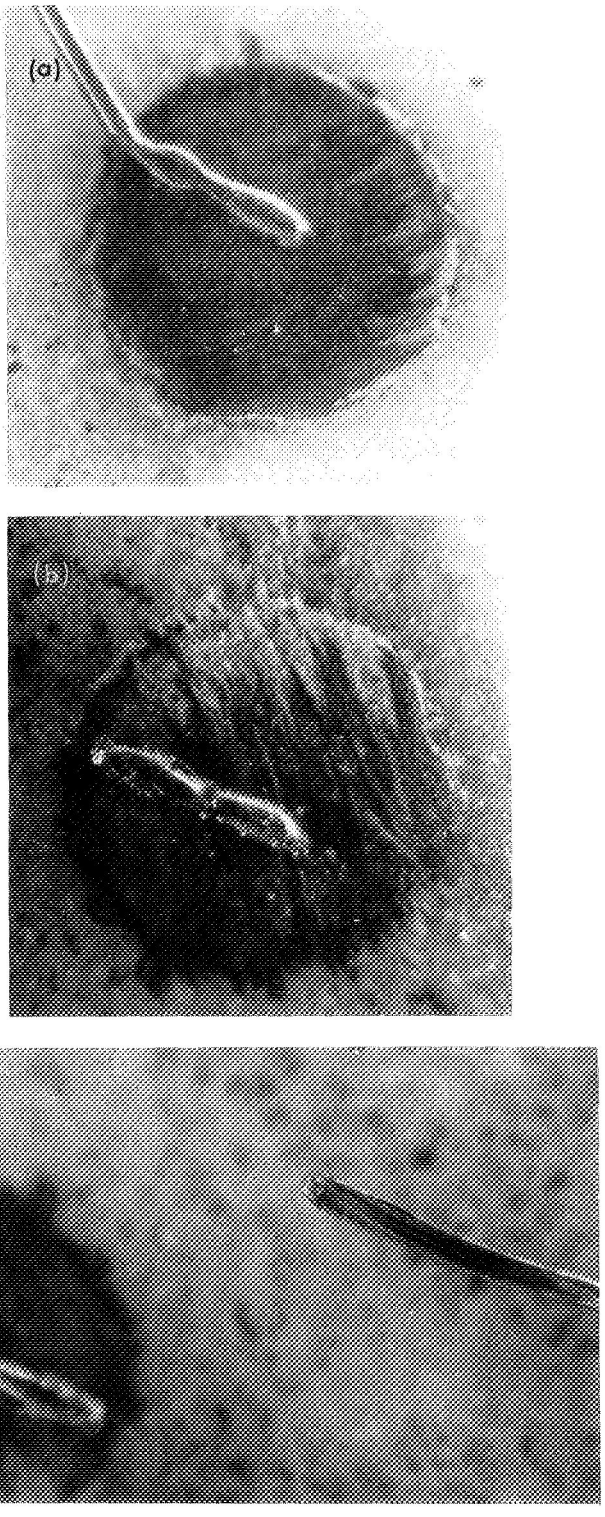

Fig. 4. Photo micrographs of CD bridgewire and posts for squib #42901

B. Low-Pressure L^*-Combustion Limits, *L. D. Strand*

1. Introduction

As part of a development effort on long-burning, high-performance motors (SPS 37-63, Vol. III, pp. 188–196), several propellant variables have been investigated in an attempt to develop propellants with lower burning rates. These variables have included propellant binder, oxidizer coarseness, and the addition of a coolant additive. Since the motors being considered have rather severe conditions at propellant ignition with regard to propellant combustion stability, i.e., low L^* (motor free volume to nozzle throat area ratio) and chamber pressure, tests were performed to determine how these propellant variables affected the low-pressure/L^* extinction limit. The tests were performed in the 7.62×10^{-2} m (3 in.) ID test motor in the same manner as described in SPS 37-41, Vol. IV, pp. 85–91, and in Ref. 1.

2. Test Results

Three propellants were examined, each one containing 16% Al and ammonium perchlorate as the oxidizer: (1) Saturethane, with a saturated polybutadiene binder and the standard bi-modal oxidizer distribution (70% coarse—170-μm mass median diam, 30% fine—17-μm mass median diam); (2) JPL 540J, with the standard JPL 540 polyether–polyurethane binder, but a tri-modal oxidizer distribution (50%—400 μm, 34%—200 μm, 16%—50 μm), and (3) EB-81, similar to JPL 540J, but containing 2½% of a burning rate suppressant, oxamide (one-half substituted for binder, one-half for oxidizer).

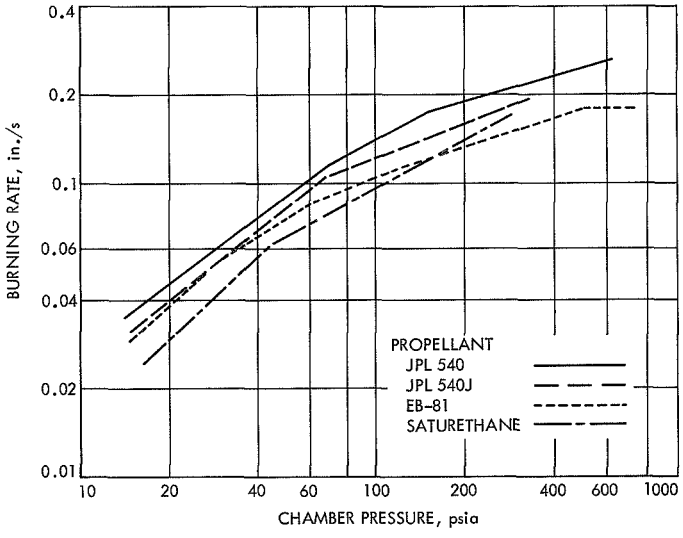

Fig. 1. Strand bomb burning rate vs pressure data

Strand bomb burning rate versus pressure data for the three propellant formulations are compared with the control JPL 540 propellant data (Fig. 1). In the pressure region of 6.9×10^5–10.3×10^5 N/m^2 (100–150 psia), the propellants, in order of descending burning rates, are JPL 540, JPL 540J, EB-81, and Saturethane. The curves for the latter two propellants cross over at approximately 10.3×10^5 N/m^2 (150 psia).

Figures 2–4 show the measured L^* versus mean chamber pressure at combustion extinction data for Saturethane, JPL 540J, and EB-81, respectively. The Saturethane data fell about the curve for JPL 540 (Fig. 2). Figure 3 shows that the tri-modal oxidizer in the JPL 540J propellant lowered the extinction pressure boundary approximately 4.1×10^4 N/m^2 (6 psi) below that of JPL 540. The addition of the oxamide to the tri-modal oxidizer propellant had a rather strong effect, raising the extinction pressure boundary approximately 6.9×10^4 N/m^2 (10 psi) so that it exceeded that of JPL 540 as well (Fig. 4). As can be seen from Fig. 4, the slopes of the curves for the different propellants are almost identical. This is in agreement with the conclusion of Ref. 1 that the slope of the L^*–$P_{c_{ex}}$ relationship is affected

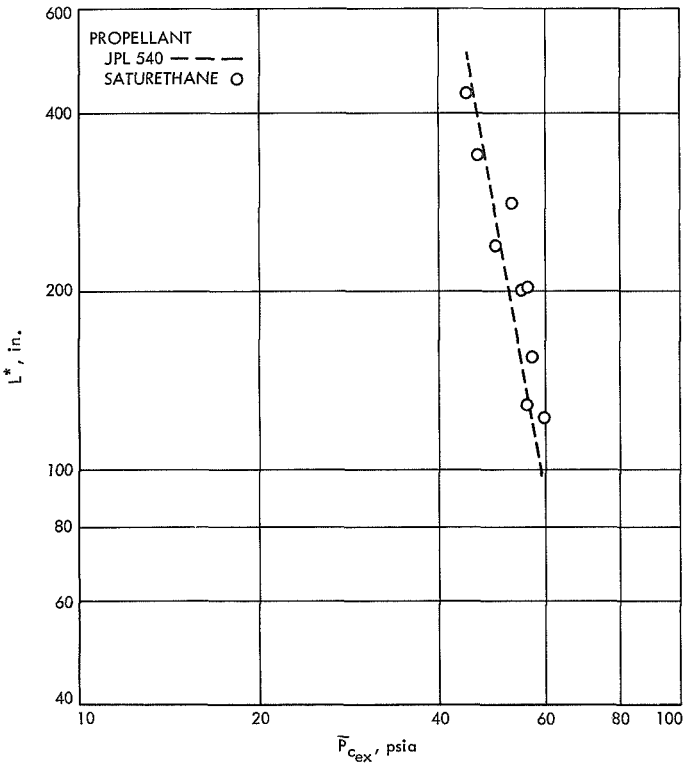

Fig. 2. L^* vs mean chamber pressure at combustion extinction $\bar{P}_{c_{ex}}$ (saturethane propellant)

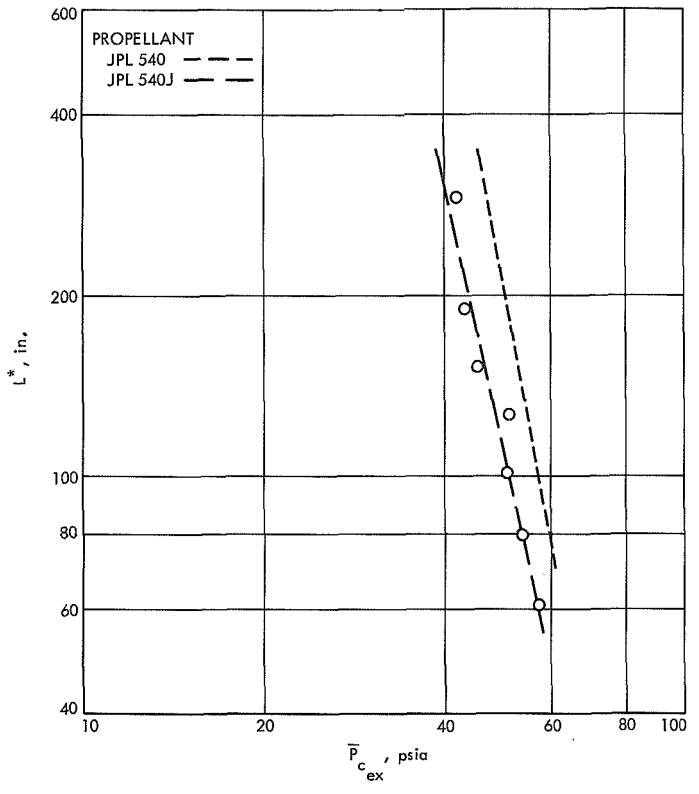

Fig. 3. L^* vs mean chamber pressure at combustion extinction $\bar{P}_{c_{ex}}$ (JPL 540J propellant)

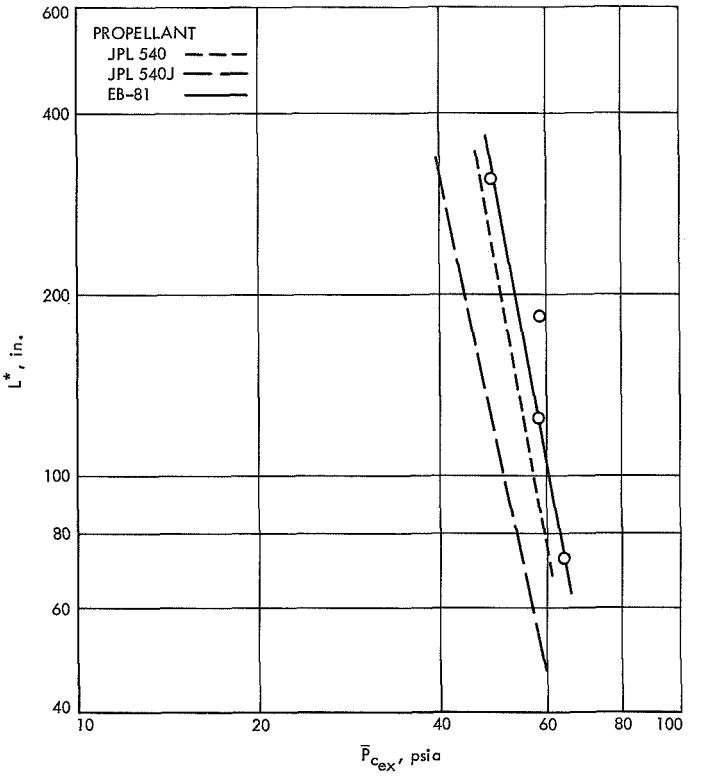

Fig. 4. L^* vs mean chamber pressure at combustion extinction $\bar{P}_{c_{ex}}$ (EB-81 propellant)

principally by the presence of aluminum, the concentration of aluminum, and the particle size of the aluminum in the propellant.

3. Discussion

In Ref. 1, a theoretical analysis, based on a highly simplified combustion model, was presented which predicted a relationship between the ease of extinguishment and propellant burning rate, namely, that the greater the low-pressure burning rate of a propellant, the lower were the motor L^*s and pressures required before combustion instability and extinction would occur. Listing the propellants tested in the order of ascending L^*-extinction pressure limit yields the following: JPL 540J, JPL 540 and Saturethane about equal, and EB-81. Referring to Fig. 1, it is obvious that the simple burning rate/stability relationship does not hold rigorously. Other factors must be considered, such as the nature of the binder decomposition, transparency of the propellant to thermal radiation, mechanisms of burning rate catalysts, and depressants, etc.

Looking at the propellants individually: Differences in binder degradation mechanisms result in Saturethane and JPL 540 propellants having essentially identical L^*-extinction boundaries, even though Saturethane has a significantly lower burning rate. The greater transparency to thermal radiation of the slower burning, coarser oxidizer JPL 540J propellant may be the reason for its greater resistance to extinguishment, as postulated in Ref. 2. Finally, the addition of coolants, such as oxamide, which supposedly decompose endothermically on or near the propellant surface, significantly raises the L^*-extinction pressure limit.

References

1. Strand, L. D., *Summary of a Study of the Low-Pressure Combustion of Solid Propellants*, Technical Report 32-1242. Jet Propulsion Laboratory, Pasadena, Calif., April 15, 1968.

2. Micheli, P. L., *A Stop-Start Study of Solid Propellants*, Final Report, Contract NAS 1-6600, NASA CR-66487. Aerojet-General Corporation, Propellant Research and Development Division, Sacramento, Calif.

C. Diffraction of a High-Order Gaussian Beam by an Aperture, *A. C. R. Livanos*[1]

1. Introduction

In a number of important laser applications, e.g., laser explosive initiation (Refs. 1 and 2), holography, etc., it is desirable to obtain uniform laser intensity distributions. Because of the inhomogeneities of the laser rod, imperfections of alignment, and multiple reflections in the optical delivery system, the output beam usually contains higher spacial frequencies. By positioning an aperture of the proper diameter, one gets rid of the intensity wings. However, by using this technique, interference rings appear in the intensity distribution.

In this article, the diffraction of a laser beam of the most general gaussian mode by an aperture is described. The beam considered is the TEM_{pln} mode[2] of a laser, which, after leaving the optical resonator, is focused by a lens and then diffracted by an aperture located at the focal point.

Huygen's principle is used to calculate the near- and far-field radiation patterns. The assumptions used to simplify the diffraction integral permit a calculation for field distributions over the entire space to the right of the aperture, in contrast with the Fresnel and/or the Fraunhofer approximations.

In the work reported here, the ultimate intensity of the beam was determined as a function of the aperture size and the oscillating mode index. The results show that for all practical purposes the use of the lowest possible mode is desirable. In this case, the output looks like a simple gaussian when the aperture is large and like the Airy pattern when the aperture is small. For intermediate sizes of aperture, the intensity distribution is a mixture of the two limits.

2. Derivation of Intensity Distribution at Aperture

The resonator–lens–aperture configuration considered is sketched in Fig. 1. Given a resonator with mirrors of curvature R_1, R_2 and length L, one can find the unique gaussian which will just fit between these mirrors, assuming that the mirror aperture is larger than the spot sizes. The distribution at an arbitrary point $P(r, \theta, z)$ inside the resonator is of the form

$$U_{p\ell}(r,\theta,z) = \frac{2}{(1+\delta_{0\ell})^{1/2}}\left[\frac{p!}{\pi(\ell+p)!}\right]^{1/2}\frac{1}{w(z)}\left[\frac{(2r)^{1/2}}{w(z)}\right]^{\ell} L_p^{\ell}\left[\frac{2r^2}{w^2(z)}\right]\begin{pmatrix}\cos\\ \sin\end{pmatrix}\ell\theta\exp\left[-j\frac{\kappa}{2}\frac{r^2}{\tilde{q}(z)}\right]$$
$$\times \exp(-j\kappa z)\exp[j(2p+\ell+1)\Psi(z)] \qquad (1)$$

where

$j = (-1)^{1/2}$

κ = wave vector

λ = wavelength

p, ℓ = integer indices

L_p^{ℓ} = associated Laguerre polynomial

$$\delta_{0\ell} = \begin{cases} 1 \text{ for } \ell = 0 \\ 0 \text{ for } \ell \neq 0 \end{cases}$$

$w(z)$ = spot size at arbitrary plane z;

$$w(z) = w_0\left[1+\left(\frac{\lambda z}{\pi w_0^2}\right)^2\right]^{1/2}$$

w_0 = spot size of gaussian wave at plane $z = 0$; also referred to as waist

$\tilde{q}(z)$ = complex radius of curvature of gaussian wave at arbitrary plane z

$$\Psi(z) = \tan^{-1}\left(\frac{\lambda z}{\pi w_0^2}\right)$$

$$\frac{1}{\tilde{q}(z)} = \frac{1}{R(z)} - \frac{j\lambda}{\pi w^2(z)}$$

$$R(z) = z + \left(\frac{\pi w_0^2}{\lambda}\right)^2\left(\frac{1}{z}\right)$$

[1]The author would like to thank Dr. N. George of Caltech for his guidance and help throughout the project, and Dr. F. E. C. Culick, also of Caltech, for his assistance in expressing the manuscript in its final form.

[2]TEM=transfer electromagnetic mode.

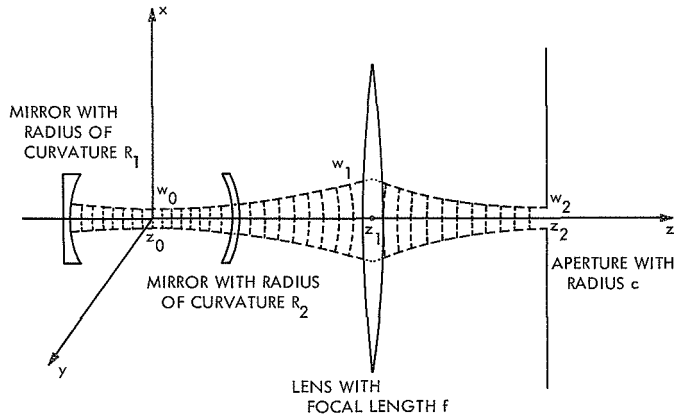

Fig. 1. Resonator–lens–aperture configuration

These symbols are the same as the ones used by Siegman (Ref. 3).

Now, if one of the mirrors is partially transparent, one can assume that the transmitted beam just before the lens will be of the same form as Eq. (1) but with reduced amplitude, and z replaced by z_1.

Immediately after the lens, the intensity distribution $U'_{p\ell}$ is

$$U'_{p\ell}(r_1, \theta_1, z_1) = t(r_1, \theta_1)\, U_{p\ell}(r_1, \theta_1, z_1) \tag{2}$$

where for an ideal lens, having focal length f, the transmittance function is

$$t(r_1, \theta_1) = B \exp\left(-j \frac{\kappa r_1^2}{2f}\right) \tag{3}$$

The finite dimensions of the lens may be accounted for if one assumes the lens to have a gaussian transmittance function of the form

$$B \exp\left(-j \frac{\kappa r_1^2}{2\rho}\right) \tag{4}$$

where

$$\frac{1}{\rho} = \frac{1}{f} + \frac{4\lambda}{i\pi D^2}$$

and where D is the lens diameter.

In the calculations that follow, the first assumption will be used. However, the results obtained by using the second kind of transmittance function are equivalent, since a gaussian when Fourier-transformed will again yield a gaussian. Thus, $U'_{p\ell}(r_1, z_1)$ is the same as $U_{p\ell}(r_1, z_1)$ but with $\tilde{q}(z_1)$ being replaced by $\tilde{q}^1(z)$ where

$$\frac{1}{\tilde{q}^1(z_1)} = \frac{1}{\tilde{q}(z_1)} + \frac{1}{f} \tag{5}$$

At point $z_2 = z_1 + f$, it can be shown, for example, by use of the Collins chart, that the wave will be a plane wave with waist w_2 (w_i = spot size of plane $z = z_i$) given by

$$w_2 = \frac{\left[1 + \left(\frac{\lambda z_1}{\pi w_0^2}\right)^2\right]^{1/2}}{\left[1 + \left(\frac{w_0^4 \pi^2 + \lambda^2 z_1^2}{\lambda \pi w_0^2 S_1}\right)^2\right]^{1/2}} \tag{6}$$

where

$$S_1 = \frac{f\left[z_1 + \left(\frac{\pi w_0^2}{\lambda}\right)\frac{1}{z_1}\right]}{f + z_1 + \left(\frac{\pi w_0^2}{\lambda}\right)^2 \frac{1}{z_1}} \tag{7}$$

Thus, the spot size at the focal point can be expressed in terms of z_1, f_1, w_0, which are all known parameters. The distribution at the aperture will then be of the form

$$U_{p\ell}(r_2, \theta_2) = \frac{A}{(1 + \delta_{0\ell})^{1/2}} \left[\frac{p!}{\pi(\ell + p)!}\right]^{1/2} \left[\frac{(2)^{1/2}}{w_2}\right]^{\ell} r_0^{\ell} L_p^{\ell}\left(\frac{2r_2^2}{w_2}\right) \exp(i\ell\theta_2) \exp\left(\frac{-r_2^2}{w_2^2}\right) \tag{8}$$

3. Derivation of Intensity Distribution at Observation Plane

Computation of the intensity at the screen is based on direct application of Huygen's principle and inclusion of a pupil function for the aperture.

$$U(P) = \frac{1}{j\lambda} \int_S U(P_2) \frac{\exp(-j\kappa R)}{\bar{R}} \cos(\bar{n},\bar{R})\, dS \qquad (9)$$

Assuming that

$$r^2 + z^2 \ll r_2^2 \qquad \text{(Fig. 2)}$$

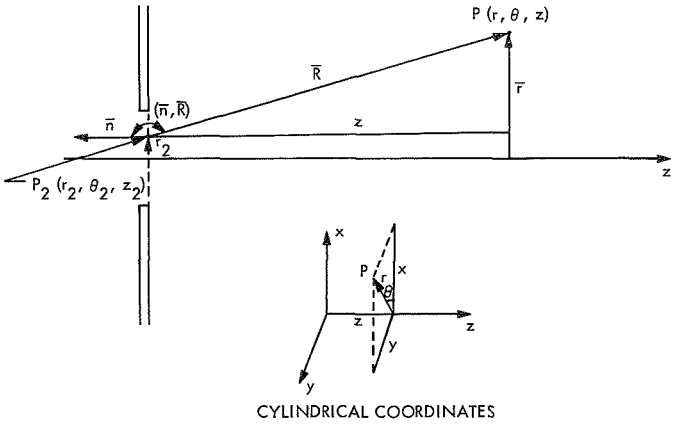

Fig. 2. Geometry of relationship between aperture and observation plane

and expanding R, one obtains

$$U(P) = \frac{jz}{\lambda} \exp\left[-j\kappa(r^2 + z^2)^{1/2}\right] \int_S\int \frac{U(P_2)}{R^2} \exp\left\{-j\kappa\left[\frac{r_2^2}{2(r^2 + z^2)^{1/2}} - \frac{rr_2\cos(\theta - \theta_2)}{(r^2 + z^2)^{1/2}}\right]\right\} r_2\, dr_2\, d\theta_2 \qquad (10)$$

where z_2 has been set equal to zero. In the exponent, only the second term of the binomial expansion was kept. The next order term is much less than 1 rad, for all cases in which r_2^2 is much less than r^2 or z^2 or their sum. Substituting Eq. (8) into Eq. (10), and by approximating R^2 by $(r^2 + z^2)$, permitted under the above assumptions, one obtains

$$U_{p\ell} = \frac{jz\exp\left[-j\kappa(r^2 + z^2)^{1/2}\right]}{\lambda(r^2 + z^2)} \frac{A}{(1 + \delta_{0\ell})^{1/2}} \left[\frac{p!}{\pi(\ell + p)!}\right]^{1/2} \left[\frac{(2)^{1/2}}{w_2}\right]^{\ell}$$

$$\times \int_0^{2\pi}\int_0^{\infty} r_2^{\ell} L_p^{\ell}\left(\frac{2r_2^2}{w_2^2}\right) \exp\left(\frac{-r_2^2}{w_2^2}\right) \exp(i\ell\theta_2) \exp\left\{-j\kappa \frac{r_2^2}{2(r^2 + z^2)^{1/2}}\right\} \exp\left\{\frac{j\kappa r r_2\cos(\theta - \theta_2)}{(r^2 + z^2)^{1/2}}\right\} r_2\, dr_2\, d\theta_2 \qquad (11)$$

Performing the integration over θ_2, and including the pupil function which will just change the limits of integration over r_2, one obtains

$$U_{p\ell}(r,z) = \frac{jz\exp\left[-j\kappa(r^2 + z^2)^{1/2}\right]}{\lambda(r^2 + z^2)} \frac{A}{(1 + \delta_{0\ell})^{1/2}} \frac{p!}{[\pi(\ell + p)!]^{1/2}} \left[\frac{(2)^{1/2}}{w_2^2}\right]^{\ell}$$

$$\times \int_0^{c} r_2^{1+\ell}\, \mathcal{J}_{\ell}\left[\frac{\kappa r r_2}{(r^2 + z^2)^{1/2}}\right] L_p^{\ell}\left(\frac{2r_2^2}{w_2^2}\right) \exp\left\{-r_2^2\left[\frac{1}{w_2^2} + \frac{j\kappa}{2(r^2 + z^2)^{1/2}}\right]\right\} dr_2 \qquad (12)$$

where $\mathcal{J}_{\ell}$ is the Bessel function of integer order of the first kind.

Let

$$G = \int_0^{c} r_2^{1+\ell}\, \mathcal{J}_{\ell}\left[\frac{\kappa r r_2}{(r^2 + z^2)^{1/2}}\right] L_p^{\ell}\left(\frac{2r_2^2}{w_2^2}\right) \exp\left\{-r_2^2\left[\frac{1}{w_2^2} + \frac{j\kappa}{2(r^2 + z^2)^{1/2}}\right]\right\} dr_2 \qquad (13)$$

and

$$\frac{r_2}{c} = x, \qquad \frac{\kappa r c}{\lambda(r^2 + z^2)} = a, \qquad \left[\frac{c^2}{w_2^2} + \frac{j\pi c^2}{\lambda(r^2 + z^2)^{1/2}}\right] = \alpha, \qquad \frac{2c^2}{w_2^2} = \beta \tag{14}$$

then

$$G = c^{2+\ell} \int_0^1 L_p^\ell (\beta x^2)\, \mathcal{J}_\ell(ax) \exp(-\alpha x^2)\, x^\ell\, x dx \tag{15}$$

but

$$L_p^\ell(z) = \sum_{k=0}^{k=p} (-1)^k \binom{p+\ell}{p-k} \frac{z^k}{k!}$$

where k is an integer index.

Hence,

$$G = c^{2+\ell} \sum_{k=0}^{k=p} (-1)^k \binom{p+\ell}{p-k} \frac{\beta^k}{k!} \int_0^1 x^{2k+\ell+1}\, \mathcal{J}_\ell(ax) \exp(-\alpha x^2)\, dx \tag{16}$$

The integral may be carried out if the Bessel function is written as a power series in ax. One finds eventually that

$$G = \frac{d^\ell}{2\alpha} c^{2+\ell} (p+\ell)! \sum_{k=0}^{k=p} \frac{\zeta^k}{(\ell+k)!\,(p-k)!} \sum_{m=0}^{m=\infty} \frac{g^m \gamma(\ell+m+k+1, \alpha)}{m!\,(m+\ell)!} \tag{17}$$

where m is an integer index, $\gamma(n, z)$ is the incomplete gamma function of order n and argument z,

$$d = \frac{a}{2\alpha}, \qquad \zeta = \frac{-\beta}{\alpha}, \qquad g = \frac{-a^2}{4\alpha}$$

Substitution of Eq. (17) into Eq. (12) will yield the distribution function $U_{p\ell}$. However, since the intensity $I_{p\ell}$, defined as $|U_{p\ell}|^2$, is of interest to us by being directly measurable, the latter will be presented.

$$I_{p\ell} = M \frac{1}{4\pi} \frac{c^4 z^2}{\lambda^2(r^2+z^2)^2} \frac{p!\,(\ell+p)!}{(1+\delta_{0\ell})} h^\ell \left| \frac{1}{\alpha^{\ell+1}} \sum_{k=0}^{k=p} \frac{\zeta^k}{(\ell+k)!\,(p-k)!} \sum_{m=0}^{m=\infty} \frac{g^m \gamma(\ell+m+k+1, \alpha)}{m!\,(m+\ell)!} \right|^2 \tag{18}$$

where

$$h = \frac{c^2 a^2}{2w_2^2}, \qquad M = \text{normalization constant}$$

A number of important cases can be derived directly from Eq. (18):

(1) When $p = 0$, then Eq. (18) reduces to

$$I_{0\ell} = M \frac{1}{4\pi} \frac{c^4 z^2}{\lambda^2 (r^2 + z^2)^2} \frac{\beta^\ell}{\ell\,!\,(1 + \delta_{0\ell})} \left| \frac{e^{-\alpha}}{\alpha} \sum_{m=1}^{m=\infty} \frac{\mathcal{J}_{\ell+m}(a)}{d^m} \right|^2 \tag{19}$$

(2) When $p = \ell = 0$, then Eq. (19) reduces to

$$I_{00} = M \frac{1}{8\pi} \frac{c^4 z^2}{\lambda^2 (r^2 + z^2)^2} \left| \frac{e^{-\alpha}}{\alpha} \sum_{m=1}^{m=\infty} \frac{\mathcal{J}_m(a)}{d^m} \right|^2 \tag{20}$$

4. Conclusions

From Eq. (18), it can be seen that the intensity is a function of the $2(\ell + 2)$ power of the radius of the aperture. Thus, for practical applications, where the efficiency of the system is important, ℓ must be small. When p increases, then the number of rings or lobes increases as it is expected, except for the case of a very small aperture. But this is also undesirable, since even for $\ell = 0$ the intensity is again a function of the fourth power of the radius of the aperture. The conclusion is, therefore, that the TEM_{00} mode is the most desirable with which to work. The intensity distribution in this case, given by Eq. (20), which for a small aperture looks like the Airy pattern and for a large one looks like a simple gaussian, is the same result as the one obtained by Kauffman (Ref. 4) and Buck (Ref. 5) with a direct numerical calculation of the diffraction integral.

A computer program in Fortran IV has been prepared to calculate the intensity distribution according to the formulation presented here. Optional output in the form of graphic display is also available.

A number of characteristic plots illustrating the above-mentioned conclusions are included (Figs. 3–5).

References

1. Cox, C. H., *Uniform Laser Beam Profile Study*, under Contract No. NAS 7-744. Consumer and Technical Products Division, Owens-Illinois, Inc., Mar. 31, 1970.

2. Menichelli, V. J., Yang, L. C., *Sensitivity of Explosives to Laser Energy*, Technical Report 32-1474. Jet Propulsion Laboratory, Pasadena, Calif., Apr. 30, 1970.

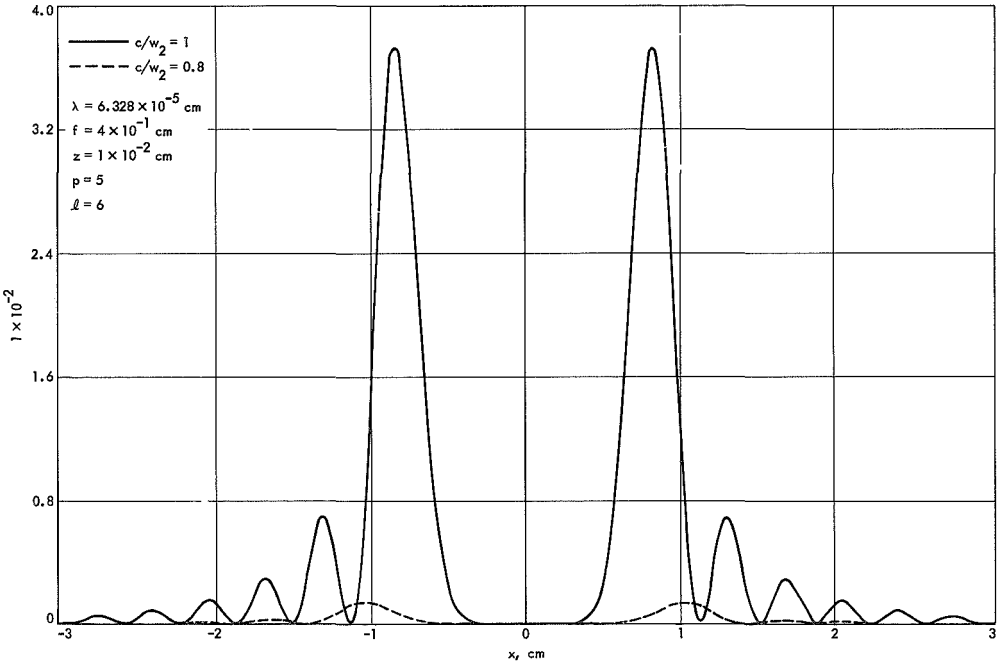

Fig. 3. Relative intensity I_{56} vs distance x from z-axis (intensity drops very fast because of high index ℓ)

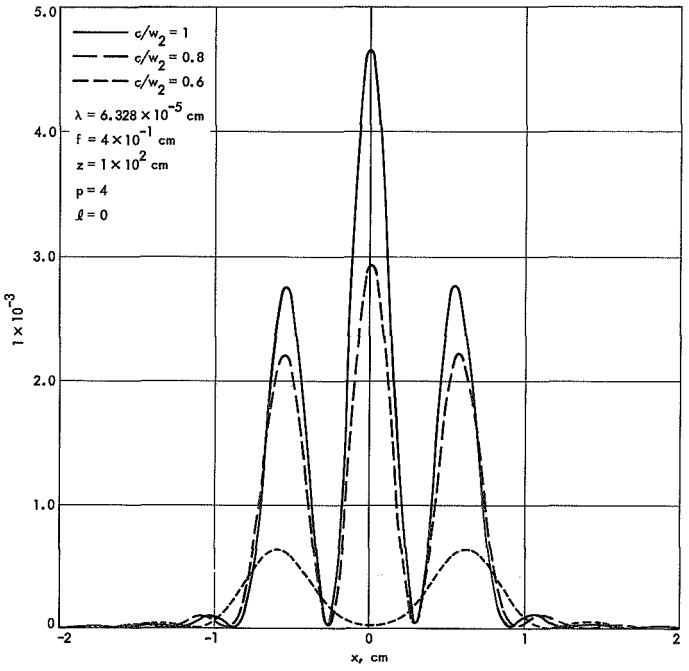

Fig. 4. Relative intensity I_{40} vs distance x from z-axis (intensity distribution exhibits number of undesirable lobes)

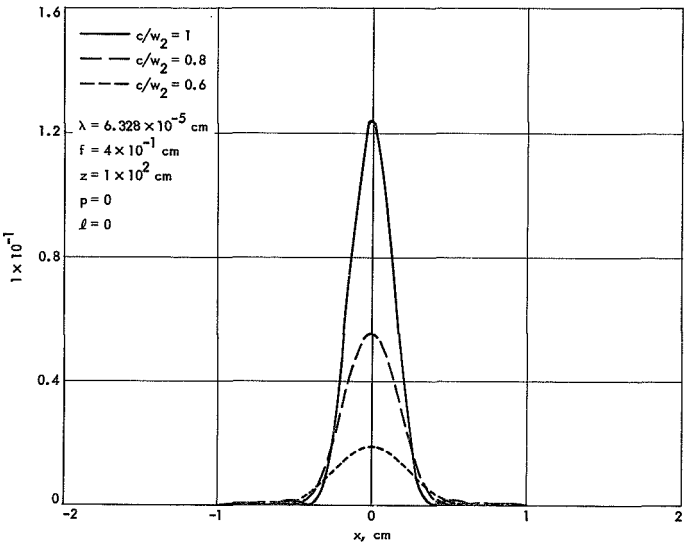

Fig. 5. Relative intensity I_{00} vs distance x from z-axis (intensity distribution exhibits very low intensity wings in comparison with maximum, which clearly illustrates desirability of this mode)

3. Siegman, A. E., *An Introduction to Lasers and Masers,* Prelim. Ed., pp. 8-15 to 8-53. McGraw-Hill Book Co., Inc., New York, 1968.

4. Kauffman, J. F., "The Calculated Radiation Patterns of a Truncated Gaussian Aperture Distribution," *IEEE Trans. Antennas and Propagation (Commun.),* Vol. AP-13, pp. 473–474, May 1965.

5. Buck, A. L., "*Radiation* Pattern of a Truncated Gaussian Aperture Distribution," *Proc. IEEE (Proc. Letters),* pp. 448–450, Mar. 1967.